Kane-Mele-Hubbard model on the π-flux honeycomb lattice

Martin Bercx,* Martin Hohenadler, and Fakher F. Assaad
Institut für Theoretische Physik und Astrophysik,
Universität Würzburg, Am Hubland, 97074 Würzburg, Germany

We consider the Kane-Mele-Hubbard model with a magnetic π flux threading each honeycomb plaquette. The resulting model has remarkably rich physical properties. In each spin sector, the noninteracting band structure is characterized by a total Chern number $C = \pm 2$. Fine-tuning of the intrinsic spin-orbit coupling λ leads to a quadratic band crossing point associated with a topological phase transition. At this point, quantum Monte Carlo simulations reveal a magnetically ordered phase which extends to weak coupling. Although the spinful model has two Kramers doublets at each edge and is explicitly shown to be a Z_2 trivial insulator, the helical edge states are protected at the single-particle level by translation symmetry. Drawing on the bosonized low-energy Hamiltonian, we predict a correlation-induced gap as a result of umklapp scattering for half-filled bands. For strong interactions, this prediction is confirmed by quantum Monte Carlo simulations.

PACS numbers: 71.10.-w, 03.65.Vf, 73.43.-f,71.27.+a

I. INTRODUCTION

The classification of insulating states of matter has been refined in terms of protecting symmetries through the discovery of topological insulators [1–4]. For example, as long as time-reversal symmetry is not broken, topological insulators cannot be adiabatically connected to non-topological band insulators without closing the charge gap [5], and the helical edge states are protected against perturbations [1, 2, 6, 7].

Recently, a further refinement was achieved by the theoretical prediction [8–10] and experimental realization [11–13] of topological crystalline insulators (TCIs). In this case, in addition to time-reversal symmetry, the two-dimensional surface has crystal symmetries which protect the topological state against perturbations. Because crystal (point group) symmetries are not defined in one dimension, this definition of TCIs requires a three-dimensional bulk and a two-dimensional surface.

Here, we introduce a two-dimensional counterpart to the TCI. In addition to time-reversal symmetry, the model we consider preserves translation symmetry at the one-dimensional edge. This leads to protection at the single-particle level despite a trivial bulk Z_2 invariant. Our model is based on the Kane-Mele (KM) model [1] on the honeycomb lattice, which has a quantum spin Hall ground state at half filling. By threading each honeycomb plaquette with a magnetic flux of size $\pm\pi$, we obtain the π *Kane-Mele (πKM) model*. The idea of inserting π fluxes has previously been considered for the case of an intensive number of fluxes [14–17], and a superlattice of well separated fluxes [18]. Isolated magnetic π fluxes locally bind zero-energy modes and lead to spin-charge separation in topological insulators [14, 15]. This property can also be exploited to identify correlated topological insulators [14, 16, 17]. Dirac fermions on the π flux square lattice have been studied in [19, 20]. Furthermore, twisted graphene multilayers have been identified as an instance of a two-dimensional TCI [21].

The physics of the πKM model is surprisingly rich. In the noninteracting case, and for each spin projection, it has Chern insulator [22] ground states characterized by Chern numbers $C = \pm 2$, separated by a topological phase transition. The band structure resembles that of the nucleated topological phase in the Kitaev honeycomb lattice model [23–25] which corresponds to the vortex sector of the Kitaev model characterized by a π flux vortex at each plaquette.

The spinful πKM model is found to have a trivial Z_2 invariant. However, there exist two pairs of helical edge states crossing at distinct points in the projected Brillouin zone, which are robust with respect to single-particle scattering processes as long as translation symmetry is preserved. An intriguing question, which we address in this manuscript using bosonization and quantum Monte Carlo methods, is if the edge states are robust to correlation effects. At half filling, we find that umklapp scattering processes between the two pairs of edge states localize the edge modes in the corresponding low-energy model, leading to a gap in the edge states without breaking translation symmetry. This prediction is consistent with quantum Monte Carlo results for the correlated edge states. Away from half filling, umklapp scattering is not relevant, and the edge states remain stable provided that translation symmetry is not broken by disorder. Finally, we investigate the bulk phase diagram of the πKM model with an additional Hubbard interaction. Our mean-field and quantum Monte Carlo results suggest the existence of a magnetic phase transition that extends to weak coupling at the quadratic band crossing point.

The paper is organized as follows. In Sec. II, we introduce the πKM model. Section III provides a brief discussion of the quantum Monte Carlo methods. The bulk properties are discussed in Sec. IV (noninteracting case) and Sec. V (interacting case). Sec. VI contains a discussion of the noninteracting edge states. The bosonization analysis of the edge states is presented in Sec. VII, followed by the quantum Monte Carlo results for correlation effects on the edge states in Sec. VIII. Finally, we conclude in Sec. IX.

II. π KANE-MELE-HUBBARD MODEL

The KM model describes electrons on the honeycomb lattice with nearest-neighbor hopping and spin-orbit coupling [1]. Given the $U(1)$ spin symmetry which conserves the z component of spin, the KM Hamiltonian reduces to two copies of the Haldane model [22, 26], one for each spin sector. The latter has an integer quantum Hall ground state or, in other words, it is a Chern insulator. The quantum spin Hall insulator results when the two Haldane models are combined in a way that restores time-reversal symmetry.

Here, we construct a new model (referred to as the πKM model) by taking the KM model and inserting a magnetic flux $\pm\pi$ into each hexagon of the underlying honeycomb lattice. Each flux can be thought of as originating from a time-reversal symmetry preserving magnetic field of the form

$$\boldsymbol{B}_{\pm}(\boldsymbol{r}) = \pi\delta(\boldsymbol{r}-\boldsymbol{r_i})(\pm)\boldsymbol{e}_z \,, \tag{1}$$

and is given by

$$\phi_{\pm} = \frac{hc}{e}\int_{\hexagon} \boldsymbol{B}_{\pm}(\boldsymbol{r})d\boldsymbol{S} = \pm\pi\frac{hc}{e}. \tag{2}$$

As illustrated in Fig. 1(a), such an arrangement of fluxes of size $\pm\pi$ (in units of hc/e) leads to a model with a unit cell consisting of two hexagons.

For each spin projection σ, the Hamiltonian takes the form of a modified Haldane model [22],

$$\begin{aligned}\mathcal{H}^{\sigma} = &-\sum_{\langle \boldsymbol{i},\boldsymbol{j}\rangle}\left[t(\boldsymbol{i},\boldsymbol{j})-\mu\delta_{\boldsymbol{ij}}\right]\hat{c}^{\dagger}_{\boldsymbol{i},\sigma}\hat{c}_{\boldsymbol{j},\sigma} \\ &+i\sigma\sum_{\langle\langle \boldsymbol{i},\boldsymbol{j}\rangle\rangle}\lambda(\boldsymbol{i},\boldsymbol{j})\nu_{\boldsymbol{i},\boldsymbol{j}}\hat{c}^{\dagger}_{\boldsymbol{i},\sigma}\hat{c}_{\boldsymbol{j},\sigma}\,.\end{aligned} \tag{3}$$

Here, $t(\boldsymbol{i},\boldsymbol{j}) = t\tau_{\boldsymbol{i},\boldsymbol{j}}$ and $\lambda(\boldsymbol{i},\boldsymbol{j}) = \lambda\tau_{\boldsymbol{i},\boldsymbol{j}}$ are the nearest-neighbor and next-nearest-neighbor hopping parameters, respectively; $\boldsymbol{i},\boldsymbol{j}$ index both lattice and orbital sites and μ is the chemical potential. The factor $\nu_{\boldsymbol{i},\boldsymbol{j}}$ is -1 $(+1)$ for $\boldsymbol{i},\boldsymbol{j}$ indexing the orbitals 1 or 3 (2 or 4).

The additional, nonuniform hopping phase factors $\tau_{\boldsymbol{i},\boldsymbol{j}} = \pm 1$ account for the presence of the π fluxes. A π flux is inserted in a honeycomb plaquette by choosing the phase factors $\tau_{\boldsymbol{i},\boldsymbol{j}}$ in such a way that their product along a closed contour around the plaquette is

$$\tau_{\boldsymbol{i},\boldsymbol{j}}\tau_{\boldsymbol{j},\boldsymbol{k}}\cdots\tau_{\boldsymbol{l},\boldsymbol{i}} = -1\,. \tag{4}$$

In a periodic system, π fluxes can only be inserted in pairs. Each hopping process from $\boldsymbol{i}$ to $\boldsymbol{j}$ that crosses the connecting line of a flux pair acquires a phase $\tau_{\boldsymbol{i},\boldsymbol{j}} = -1$, which fixes the position of both fluxes according to Eq. (4). In general, there is no one-to-one correspondence between the flux positions and the set of $\tau_{\boldsymbol{i},\boldsymbol{j}}$, i.e., one eventually has to make a gauge choice. Due to the geometry of the four-orbital unit cell, two gauges exist [see Fig. 1(a)] which have unitarily equivalent Hamiltonians.

On a torus geometry, Hamiltonian (3) becomes

$$\mathcal{H}^{\sigma} = \sum_{\boldsymbol{k}} c^{\dagger}_{\boldsymbol{k},\sigma}H^{\sigma}(\boldsymbol{k})c_{\boldsymbol{k},\sigma}\,, \tag{5}$$

where $c_{\boldsymbol{k},\sigma} = (\hat{c}_{1,\boldsymbol{k},\sigma},\hat{c}_{3,\boldsymbol{k},\sigma},\hat{c}_{2,\boldsymbol{k},\sigma},\hat{c}_{4,\boldsymbol{k},\sigma})^T$ is the basis in which the nearest-neighbor term is block off-diagonal. The Hamilton matrix $H^{\sigma}(\boldsymbol{k})$ can be expressed in terms of Dirac Γ matrices [1], $\Gamma^{(1,2,3,4,5)} = (\sigma_x\otimes\mathbb{1}, \sigma_z\otimes\mathbb{1}, \sigma_y\otimes\sigma_x, \sigma_y\otimes\sigma_y, \sigma_y\otimes\sigma_z)$ and their commutators $\Gamma^{ab} = [\Gamma^a,\Gamma^b]/(2i)$:

$$H^{\sigma}(\boldsymbol{k}) = \mu\,\mathbb{1} + \sum_{a=1}^{5} d_a(\boldsymbol{k})\Gamma^a + \sum_{a<b=1}^{5} d^{\sigma}_{ab}(\boldsymbol{k})\Gamma^{ab}\,. \tag{6}$$

The nonvanishing coefficients $d_a(\boldsymbol{k})$ and $d^{\sigma}_{ab}(\boldsymbol{k})$ are given in Table I.

As for the KM model, a spinful and time-reversal invariant Hamiltonian results by combining $\mathcal{H}^{\uparrow}$ and $\mathcal{H}^{\downarrow}$; λ then plays the role of an intrinsic spin-orbit coupling. Including a Rashba spin-orbit interaction which breaks the $U(1)$ spin symmetry, we have

$$\begin{aligned}\mathcal{H}_0 = &-\sum_{\langle \boldsymbol{i},\boldsymbol{j}\rangle,\sigma}\left[t(\boldsymbol{i},\boldsymbol{j})-\mu\delta_{\boldsymbol{i},\boldsymbol{j}}\right]\hat{c}^{\dagger}_{\boldsymbol{i},\sigma}\hat{c}_{\boldsymbol{j},\sigma} \\ &+i\sum_{\langle\langle \boldsymbol{i},\boldsymbol{j}\rangle\rangle,\sigma}\sigma\lambda(\boldsymbol{i},\boldsymbol{j})\nu_{\boldsymbol{i},\boldsymbol{j}}\hat{c}^{\dagger}_{\boldsymbol{i},\sigma}\hat{c}_{\boldsymbol{j},\sigma} \\ &+i\sum_{\langle \boldsymbol{i},\boldsymbol{j}\rangle}\left(\hat{c}^{\dagger}_{\boldsymbol{i},\uparrow},\hat{c}^{\dagger}_{\boldsymbol{i},\downarrow}\right)\lambda_{\mathrm{R}}(\boldsymbol{i},\boldsymbol{j})\boldsymbol{e}_z(\boldsymbol{\sigma}\times\boldsymbol{d}_{\boldsymbol{i},\boldsymbol{j}})\begin{pmatrix}\hat{c}_{\boldsymbol{j},\uparrow}\\ \hat{c}_{\boldsymbol{j},\downarrow}\end{pmatrix}\,.\end{aligned} \tag{7}$$

In the Rashba term, $\lambda_{\mathrm{R}}(\boldsymbol{i},\boldsymbol{j}) = \lambda_{\mathrm{R}}\tau_{\boldsymbol{ij}}$, $\boldsymbol{d}_{\boldsymbol{i},\boldsymbol{j}}$ is a vector pointing to one of the three nearest-neighbor sites, and $\boldsymbol{\sigma} = (\sigma^x,\sigma^y,\sigma^z)$ is the vector of Pauli matrices.

Taking into account a Hubbard term to model electron-electron interactions, we finally arrive at the Hamiltonian of the π Kane-Mele-Hubbard (πKMH) model,

$$\mathcal{H} = \mathcal{H}_0 + U\sum_{\boldsymbol{i}}\hat{n}_{\boldsymbol{i},\uparrow}\hat{n}_{\boldsymbol{i},\downarrow}\,. \tag{8}$$

III. QUANTUM MONTE CARLO METHODS

The πKMH lattice model can be studied using the auxiliary-field determinant quantum Monte Carlo method. Simulations are free of a sign problem given particle-hole, time-reversal and $U(1)$ spin symmetry [27–29]. This requirement excludes the $U(1)$ spin symmetry breaking Rashba term. The algorithm has been discussed in detail previously [29, 30]. To study the magnetic phase diagram of the πKMH model, we apply a finite-temperature implementation [30]. The Trotter discretization was chosen as $\Delta\tau t = 0.1$. An inverse temperature $\beta t = 40$ was sufficient to obtain converged results.

Interaction effects on the helical edge states can be studied numerically by taking advantage of the exponential localization of the edge states and of the insulating

$d_1(\boldsymbol{k}) = -t\cos(\boldsymbol{k}\boldsymbol{a}_2)$	$d^\sigma_{12}(\boldsymbol{k}) = t\sin(\boldsymbol{k}\boldsymbol{a}_2)$	$d^\sigma_{23}(\boldsymbol{k}) = t\cos(\boldsymbol{k}\boldsymbol{a}_1/2)\cos(\boldsymbol{k}(\boldsymbol{a}_1/2-\boldsymbol{a}_2))$
$d_3(\boldsymbol{k}) = -\frac{t}{2}\big[\sin(\boldsymbol{k}\boldsymbol{a}_2)-\sin(\boldsymbol{k}(\boldsymbol{a}_1-\boldsymbol{a}_2))\big]$	$d^\sigma_{13}(\boldsymbol{k}) = -2\sigma\lambda\sin(\boldsymbol{k}\boldsymbol{a}_1/2)\cos(\boldsymbol{k}\boldsymbol{a}_1/2)$	$d^\sigma_{24}(\boldsymbol{k}) = \frac{t}{2}\big[\sin(\boldsymbol{k}(\boldsymbol{a}_1-\boldsymbol{a}_2))+\sin(\boldsymbol{k}\boldsymbol{a}_2)\big]$
$d_4(\boldsymbol{k}) = -\frac{t}{2}\big[\cos(\boldsymbol{k}(\boldsymbol{a}_1-\boldsymbol{a}_2))-\cos(\boldsymbol{k}\boldsymbol{a}_2)\big]$	$d^\sigma_{14}(\boldsymbol{k}) = -2\sigma\lambda\sin^2(\boldsymbol{k}\boldsymbol{a}_1/2)$	$d^\sigma_{35}(\boldsymbol{k}) = 2\sigma\lambda\cos(\boldsymbol{k}\boldsymbol{a}_1/2)\cos(\boldsymbol{k}(\boldsymbol{a}_1/2-\boldsymbol{a}_2))$
$d_{25}(\boldsymbol{k}) = t$	$d^\sigma_{15}(\boldsymbol{k}) = 2\sigma\lambda\sin(\boldsymbol{k}\boldsymbol{a}_2)$	$d^\sigma_{45}(\boldsymbol{k}) = 2\sigma\lambda\cos(\boldsymbol{k}(\boldsymbol{a}_1/2-\boldsymbol{a}_2))\sin(\boldsymbol{k}\boldsymbol{a}_1/2)$

TABLE I. Nonzero coefficients $d_a(\boldsymbol{k})$ and $d^\sigma_{ab}(\boldsymbol{k})$ of Eq. (6).

nature of the bulk which has no low-energy excitations. Accordingly, the low-energy physics is captured by considering the Hubbard term only for the edge sites at one edge of a (zigzag) ribbon. The bulk therefore is considered noninteracting and establishes the topological band structure; it plays the role of a fermionic bath. The resulting model is simulated without further approximations using the continuous-time quantum Monte Carlo algorithm based on a series expansion in the interaction U (CT-INT) [31]. A similar approach has previously been used to study edge correlation effects in the KMH model [27, 32]. Compared to the KMH model, the Rashba term leads to a moderate sign problem.

IV. BULK PROPERTIES OF THE πKM MODEL

In this section, we discuss the band structure and the topological phases of the noninteracting model (5), corresponding to one spin sector of the πKM model. Subsequently, we show that the spinful πKM model (7) is Z_2 trivial at half filling.

A. Band structure

The band structure is established by the eigenvalues of Eq. (5) which are, for $\mu = 0$, given by

$$E_m(\boldsymbol{k}) = \pm\Big\{3t^2+6\lambda^2-2\lambda^2 f(\boldsymbol{k}) \pm t\sqrt{2\big[3\big(t^2+8\lambda^2\big)+\big(t^2-16\lambda^2\big)f(\boldsymbol{k})\big]}\Big\}^{1/2}, \tag{9}$$

where $f(\boldsymbol{k}) = \cos(\boldsymbol{k}\boldsymbol{a}_1)+\cos(2\boldsymbol{k}\boldsymbol{a}_2)-\cos[\boldsymbol{k}(2\boldsymbol{a}_2-\boldsymbol{a}_1)]$. At $\lambda = 0$, $\mathcal{H}^\sigma$ has four distinct Dirac points $\boldsymbol{K}_i$ with linear dispersion at zero energy,

$$E(\boldsymbol{K}_i+\boldsymbol{k}) = \sqrt{\frac{3}{2}}t\,(k_x+k_y)+\mathcal{O}(k^2)\,, \tag{10}$$

where $\boldsymbol{K}_{1,2} = (\pi/3)(1,\pm 2/\sqrt{3})$, $\boldsymbol{K}_3 = (\pi/3)(2,5/\sqrt{3})$ and $\boldsymbol{K}_4 = (\pi/3)(2,1/\sqrt{3})$. At $\lambda/t = 1/2$, the spectral gap closes quadratically at two points $\boldsymbol{\Gamma}_i$,

$$E(\boldsymbol{\Gamma}_i+\boldsymbol{k}) = \frac{3\sqrt{3}}{4}t\,\big(k_x^2+k_y^2\big)+\mathcal{O}(k^4)\,, \tag{11}$$

where $\boldsymbol{\Gamma}_1 = (\pi/3)(1,0)$ and $\boldsymbol{\Gamma}_2 = (\pi/3)(2,\sqrt{3})$ (Fig. 1). For the spinful model (7) with nonzero Rashba coupling, the point of quadratic band crossing is replaced by a finite region with zero band gap.

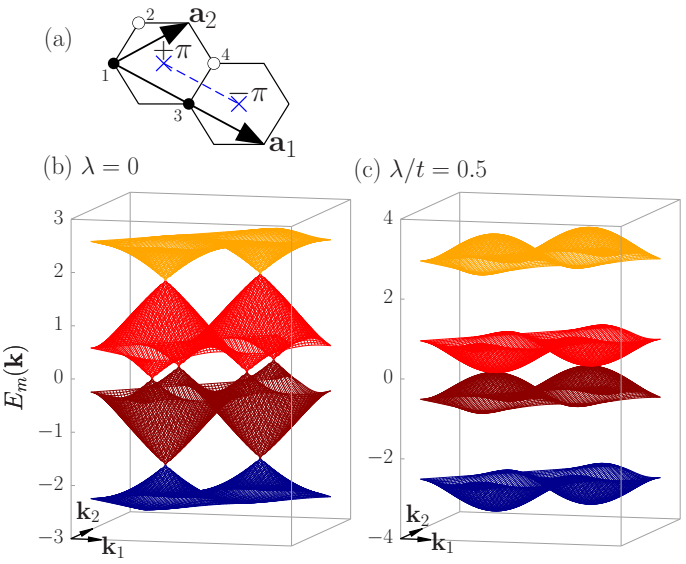

FIG. 1. (Color online) (a) The unit cell of the π flux honeycomb lattice has four orbitals and is defined by the lattice vectors $\boldsymbol{a}_1 = \big(3,-\sqrt{3}\big)$ and $\boldsymbol{a}_2 = \frac{1}{2}\big(3,\sqrt{3}\big)$. Each honeycomb plaquette carries a magnetic flux $\pm\pi$. The flux positions, defined by Eq. (4), are fixed by requiring that hopping terms crossing the dashed blue line (which is a gauge choice) acquire a phase of -1. The eigenvalue spectrum $E_m(\boldsymbol{k})$ of $\mathcal{H}^\sigma$ [Eq. (3)] has (b) four Dirac cones at $\lambda = 0$, and (c) two points of quadratic band crossing at $\lambda/t = 0.5$.

B. Quantized Hall conductivity

We first consider the Chern insulator defined by $H(\boldsymbol{k})$ in Eq. (5). In this case, the electromagnetic response reveals the topological properties of the band structure. In linear response to an external vector potential, the optical conductivity tensor of an n-band noninteracting system described by a Hamilton matrix $H(\boldsymbol{k})$ is given by

$$\sigma_{\alpha,\beta}(\omega) = \frac{1}{N}\frac{(e/\hbar)^2}{i(\omega+i0^+)}\left[\langle K_\alpha\rangle\delta_{\alpha,\beta}-\Lambda_{\alpha,\beta}(\omega)\right], \tag{12}$$

where

$$\langle K_\alpha\rangle = \sum_{\boldsymbol{k},n} f[E_n(\boldsymbol{k})]\mathrm{Tr}[K_\alpha(\boldsymbol{k})P_n(\boldsymbol{k})]\,,$$

$$\Lambda_{\alpha,\beta}(\omega) = \sum_{\boldsymbol{k},m,n}\lambda_{mn}(\boldsymbol{k},\omega)\mathrm{Tr}[J_\alpha(\boldsymbol{k})P_n(\boldsymbol{k})J_\beta(\boldsymbol{k})P_m(\boldsymbol{k})]\,,$$

$$\lambda_{mn}(\boldsymbol{k},\omega) = \frac{f[E_m(\boldsymbol{k})]-f[E_n(\boldsymbol{k})]}{\omega+i0^++E_m(\boldsymbol{k})-E_n(\boldsymbol{k})}\,, \tag{13}$$

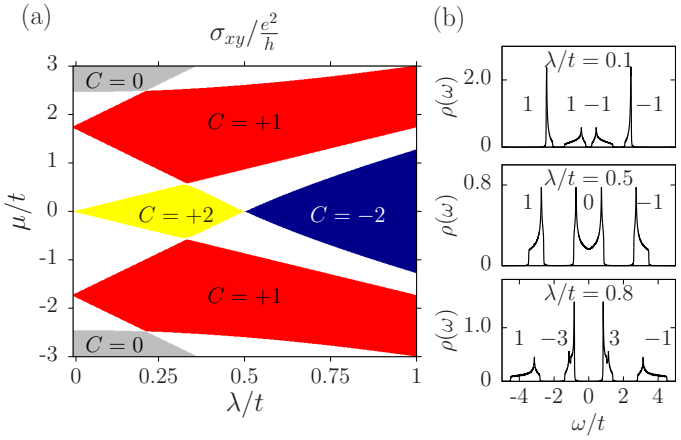

FIG. 2. (Color online) (a) Total Chern number $C=\sum_n C_n$ of the occupied bands of $\mathcal{H}^{\downarrow}$ [Eq. (3)], as obtained from the Hall conductivity σ_{xy} in the insulating phases which are separated by metallic regions (white). (b) Density of states $\rho(\omega)=(1/4N)\sum_{\boldsymbol{k},n}\delta(\omega-E_n(\boldsymbol{k}))$ and Chern numbers C_n of the individual bands.

using the matrices $J_\alpha(\boldsymbol{k})=\partial H(\boldsymbol{k})/\partial k_\alpha$, $K_\alpha(\boldsymbol{k})=-\partial^2 H(\boldsymbol{k})/\partial k_\alpha^2$, the projector on the n-th band $P_n(\boldsymbol{k})$, and the Fermi function $f[E_n(\boldsymbol{k})]$. The Hall conductivity is then computed by taking the zero-frequency limit of the optical conductivity,

$$\lim_{\omega\to 0}\mathrm{Re}\left[\sigma_{xy}(\omega)\right]=\sigma_{xy}=\left[\sum_{n=1}^{N_{\mathrm{occ}}}C_n\right]\frac{e^2}{h}\,. \tag{14}$$

It directly measures the (first) Chern number C of the gap, which is the sum of the Chern numbers C_n of the N_{occ} occupied bands. Figure 2 shows the Chern number as a function of the chemical potential μ and the ratio t_2/t_1. Transitions between different Chern insulators are topological phase transitions and necessarily involve an intermediate metallic state where the Chern number can in principle take any value. Of particular interest for the understanding of correlation-induced instabilities is the transition at $\mu=0$ as a function of t_2/t_1 between the states with $C=\pm 2$. At $t_2/t_1=1/2$, we find a a quadratic band crossing point with a nonzero density of states.

For the spinful model (7) with $U=0$ and a $U(1)$ spin symmetry ($\lambda_{\mathrm{R}}=0$), one can define a quantized spin Hall conductivity σ^s_{xy} in terms of the Hall conductivity σ^σ_{xy} of $\mathcal{H}^\sigma$ (5). At $\mu=0$, σ^σ_{xy} and σ^s_{xy} take the values

$$\sigma^\sigma_{xy}=\mp\sigma 2\frac{e^2}{h}\,,\quad \sigma^s_{xy}=\frac{\hbar}{2e}\left(\sigma^\uparrow_{xy}-\sigma^\downarrow_{xy}\right)=\mp 2\frac{e}{2\pi}\,. \tag{15}$$

The sign change occurs at the quadratic band crossing point at $\lambda/t=\lambda_0=1/2$.

C. Z_2 invariant

In the general case where the $U(1)$ spin symmetry is broken, for example by the presence of a Rashba term, the topological properties of a system with time-reversal symmetry are determined by the Z_2 topological invariant [2]. Recently, it was shown that the Z_2 index can be calculated with a manifestly gauge-independent method that only relies on time-reversal symmetry [33, 34]. The idea is to consider the adiabatic change of one component of the reciprocal lattice vector, say k_y, along high-symmetry paths $k_y\in(k,k')$ in a rectangular Brillouin zone, while keeping the other component (k_x) fixed. This process is determined by the unitary evolution operator $U_{k,k'}$ and its differential equation

$$i\frac{\mathrm{d}}{\mathrm{d}k}U_{k,k'}=i\left[P_k,\partial_k P_k\right]U_{k,k'}\,. \tag{16}$$

The initial condition is $U_{k',k'}=P_{k'}$ and $P_k=\sum_i|u_i(k)\rangle\langle u_i(k)|$ is the projector on the occupied eigenstates of the πKM Hamiltonian. Equation (16) is integrated by evenly discretizing the path (k,k'),

$$U_{k,k'}=\lim_{N\to\infty}\prod_{n=1}^{N}P_{k'+k\frac{n-1}{N-1}}\,. \tag{17}$$

The topological invariant is then given as the product of two pseudo-invariants

$$\Xi_{2\mathrm{D}}=\pm 1=\prod_{k_x=0,\pi}\frac{\mathrm{Pf}\left[\langle u_i(0)|\theta|u_j(0)\rangle\right]}{\mathrm{Pf}\left[\langle u_i(\pi)|\theta|u_j(\pi)\rangle\right]} \times\frac{\det\left[\langle u_i(\pi)|U_{(\pi,0)}|u_j(0)\rangle\right]}{\sqrt{\det\left[\langle u_i(\pi)|U_{(\pi,-\pi)}|u_j(\pi)\rangle\right]}}\,, \tag{18}$$

where the dependence on k_x is implicit and the invariant is computed numerically [35]. In the actual implementation, one has to make sure to use the same branch for the square root at $k_x=0$ and at $k_x=\pi$. For the πKM model (7) at half filling ($\mu=0$) we obtain, as expected [6], a trivial insulator ($\Xi_{2\mathrm{D}}=+1$). In contrast, if the chemical potential lies in the lower (upper) band gap, i.e., at quarter (three-quarter) filling, we obtain a quantum spin Hall insulator ($\Xi_{2\mathrm{D}}=-1$).

It is interesting to consider how other bulk probes for the Z_2 index lead to the conclusion of a trivial insulating state at half filling. For example, the Z_2 index can be probed by looking at the response to a magnetic π flux [14, 15, 17]. In the quantum spin Hall state, threading a δ-function π flux through the lattice amounts to generating a Kramers pair of states located at the middle of the gap. Provided that the particle number is kept constant during the adiabatic pumping of the π flux, these mid-gap states give rise to a Curie law in the uniform spin susceptibility. This signature of the quantum spin Hall state has been detected in Ref. 17 in the presence of correlations. For the half-filled πKM model, the insertion

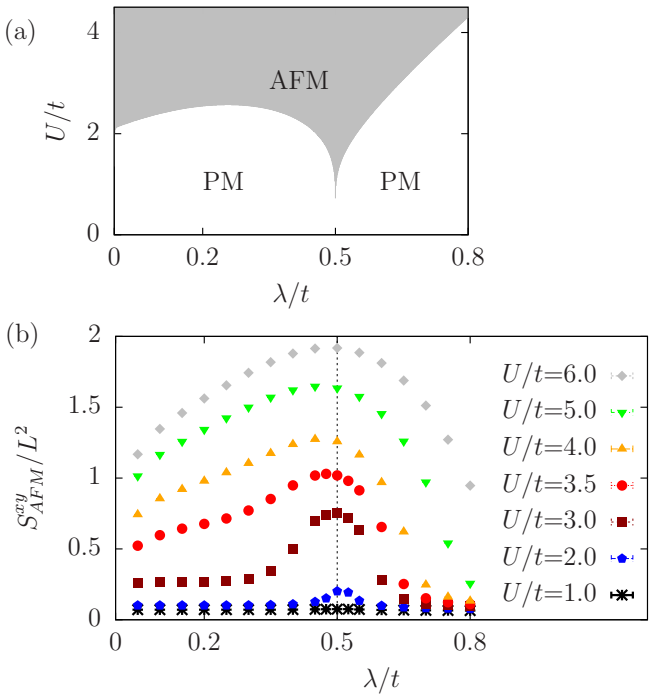

FIG. 3. (Color online) (a) Phase diagram of the mean-field Hamiltonian (19), showing the existence of a magnetically order phase with xy magnetic order above a critical value U_c that depends on the spin-orbit coupling λ. For $\lambda/t = 0.5$, where the model has a quadratic band crossing point, magnetic order exists for any nonzero value of U_c. (b) Transverse magnetic structure factor $S^{xy}_{\rm AFM}$ of the model (8) for different values U/t, as obtained from quantum Monte Carlo simulations of the πKMH model on a 6×6 lattice with periodic boundary conditions and at inverse temperature $\beta t = 40$.

of a π flux leads to a pair of Kramers degenerate states which form bonding and antibonding combinations and thereby cut off the Curie law at energy scales below the bonding-antibonding gap.

V. BULK CORRELATION EFFECTS

We begin our analysis of the effect of electron-electron interactions by considering the πKMH model (8) on a torus geometry. In order to compare our mean-field predictions to quantum Monte Carlo results, we set the Rashba spin-orbit coupling and the chemical potential to zero. The KMH model without additional π fluxes is known to exhibit long-range, transverse antiferromagnetic order at large values of U/t [27, 28, 36, 37]. We therefore decouple the Hubbard term in Eq. (8) in the spin sector, allowing for an explicit breaking of time-reversal symmetry. The mean-field Hamiltonian reads

$$\mathcal{H}_{\rm mf} = \mathcal{H}_0 - \frac{2U}{3}\sum_{\boldsymbol{i}} \left(2\hat{S}_{\boldsymbol{i}}\langle\hat{S}_{\boldsymbol{i}}\rangle - \langle\hat{S}_{\boldsymbol{i}}\rangle^2\right) + \frac{UN}{2}\,, \quad (19)$$

where $\mathcal{H}_0$ is given by Eq. (7) with $\lambda_{\rm R} = 0$, and $\hat{S}_{\boldsymbol{i}} = (\hat{S}^x_{\boldsymbol{i}}, \hat{S}^y_{\boldsymbol{i}}, \hat{S}^z_{\boldsymbol{i}})$. Assuming antiferromagnetic order, we make the ansatz $\langle\hat{S}_{\boldsymbol{i}}\rangle = S_{{\rm mf},\boldsymbol{i}}$ and

$$S^x_{{\rm mf},\boldsymbol{i}} = \nu_{\boldsymbol{i}}\, m\,, \quad S^{y,z}_{{\rm mf},\boldsymbol{i}} = 0\,,$$
$$S^x_{{\rm mf},\boldsymbol{i}} = \frac{1}{Z}\frac{1}{2}\sum_{s,s'} {\rm Tr}\left[e^{-\beta\mathcal{H}_{\rm mf}\{S^x_{{\rm mf},\boldsymbol{i}}\}}\hat{c}^\dagger_{\boldsymbol{i},s}\sigma_x\hat{c}_{\boldsymbol{i},s'}\right], \quad (20)$$

where $\nu_{\boldsymbol{i}} = +1$ ($\nu_{\boldsymbol{i}} = -1$) if $\boldsymbol{i}$ indexes the orbitals $1, 3$ $(2, 4)$. Equation (20) is solved self-consistently, resulting in the phase diagram shown in Fig. 3(a). We find a magnetic phase with transverse antiferromagnetic order above a critical value of U/t which depends on λ/t. In particular, at the quadratic band crossing point ($\lambda_0 = 0.5$), the magnetic transition occurs at infinitesimal values of U/t as a result of the Stoner instability associated with the nonvanishing density of states at the Fermi level. Tuning the system away from the quadratic band crossing point, the critical interaction increases.

To go beyond the mean-field approximation, we apply the auxiliary-field quantum Monte Carlo method discussed in Sec. III to the πKMH model. We calculate the transverse antiferromagnetic structure factor

$$S^{xy}_{\rm AFM} = \frac{1}{L^2}\sum_{\boldsymbol{i},\boldsymbol{j}}(-1)^{\nu_{\boldsymbol{i}}+\nu_{\boldsymbol{j}}}\langle\hat{S}^+_{\boldsymbol{i}}\hat{S}^-_{\boldsymbol{j}} + \hat{S}^-_{\boldsymbol{i}}\hat{S}^+_{\boldsymbol{j}}\rangle \quad (21)$$

as a function of the interaction U and the spin-orbit coupling λ. Simulations were done on a 6×6 π-flux honeycomb lattice (equivalent to 72 honeycomb plaquettes).

As shown in Fig 3(b), for small U/t, the structure factor has a clear maximum close to λ_0, where the weak-coupling magnetic instability is observed in mean-field theory. At larger values of U/t, the maximum becomes less pronounced, and the enhancement of $S^{xy}_{\rm AFM}$ for all values of λ/t is compatible with the existence of a magnetic phase for all λ/t at large U/t. These numerical results seem to confirm the overall features of the mean-field phase diagram. The numerical determination of the exact phase boundaries from a systematic finite-size scaling is left for future work.

VI. EDGE STATES OF THE πKM MODEL

We now consider the edge states of the noninteracting πKM model (7) on a zigzag ribbon with open (periodic) boundary conditions in the $\boldsymbol{a}_1$ ($\boldsymbol{a}_2$) direction [Fig. 4(a)], and with momentum $k = \boldsymbol{k}\cdot\boldsymbol{a}_2$ along the edge. Since the model is Z_2 trivial, we expect an even number of edge modes to traverse the bulk gap [6]. Furthermore, given the spin Chern number $\sigma^s_{xy}/(e/2\pi) = \pm 2$ [see Eq. (15)], we expect two helical edge modes at half filling. Figure 4(b) shows the eigenvalue spectrum with degenerate Kramers doublets at the time-reversal invariant momenta $k = 0$ and $k = \pi$. For $\lambda_0 < \lambda/t < \lambda_\pi$, where $\lambda_\pi = \sqrt{3}/2$, the eigenvalue spectrum of Eq. (3) has two additional

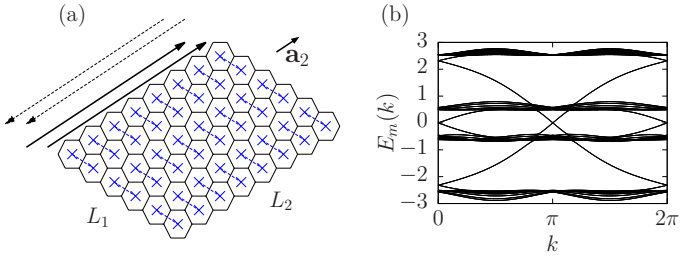

FIG. 4. (Color online) (a) Ribbon geometry of the π flux honeycomb lattice. In the spinful case, the edge states consist of two Kramers doublets with Fermi velocities v_0 and v_π. (b) Eigenvalue spectrum $E_m(k)$ of Eq. (7) for $\lambda/t = 0.3$ and $\lambda_R/t = 0.1$ on a zigzag ribbon.

cones at $k = \pi \pm \delta$. They are unstable in the sense that their existence relies on the $U(1)$ spin symmetry.

The edge modes at $k = 0$ ($k = \pi$) and $\sigma = \uparrow, \downarrow$ can be further characterized by their Fermi velocity v_0 (v_π) and—in the case of a $U(1)$ spin symmetry—by their chirality (the sign of the velocity). The chirality changes at λ_0 and λ_π. For $\lambda/t < \lambda_0$, the edge modes have the same chirality, so that the $(0, \sigma)$ modes propagate in the same direction as the (π, σ) modes. In contrast, for $\lambda_0 < \lambda/t < \lambda_\pi$, they have opposite chirality since the direction of propagation of the $(0, \sigma)$ modes is reversed after going through the point of quadratic band crossing. At $\lambda/t = \lambda_\pi$, the additional cones at $k = \pi \pm \delta$ merge with the (π, σ) modes. Consequently, the direction of propagation of the (π, σ) modes is reversed and for $\lambda/t > \lambda_\pi$ both edge modes have the same chirality again. In the limit $\lambda/t \to \infty$, v_0 and v_π become equal. Furthermore, the velocities have equal magnitude but opposite sign at $\lambda/t = \lambda_s \approx 0.665$.

To study the edge states, we consider the local single-particle spectral function

$$A_i^\sigma(k, \omega) = -\frac{1}{\pi} \mathrm{Im}\, G_{ii}^\sigma(k, \omega + i0^+) \,, \tag{22}$$

where the local noninteracting Green function is

$$G_{ii}^\sigma(k, \omega + i0^+) = \left[\omega + i0^+ - H(k)\right]^{-1}_{i\sigma, i\sigma} \,. \tag{23}$$

The edge corresponds to the orbital index $i = 2$ [Fig. 1(a)] and for brevity we will omit the index i in the following. The Fermi velocities v_0 and v_π and the local spectral function are shown in Fig. 5 [38].

Similar phases, characterized by a trivial Z_2 index and two helical edge modes at $k = 0, \pi$, have been found in the KM model with additional third-neighbor hopping terms [39], and in the anisotropic Bernevig-Hughes-Zhang model [3, 40].

In the remainder of this section, we concentrate on the low-energy properties of the πKM model (7). Furthermore, we focus on the edge modes at the time-reversal invariant momenta $k = 0, \pi$, and neglect the two additional, unstable modes at $k = \pi \pm \delta$ occurring for

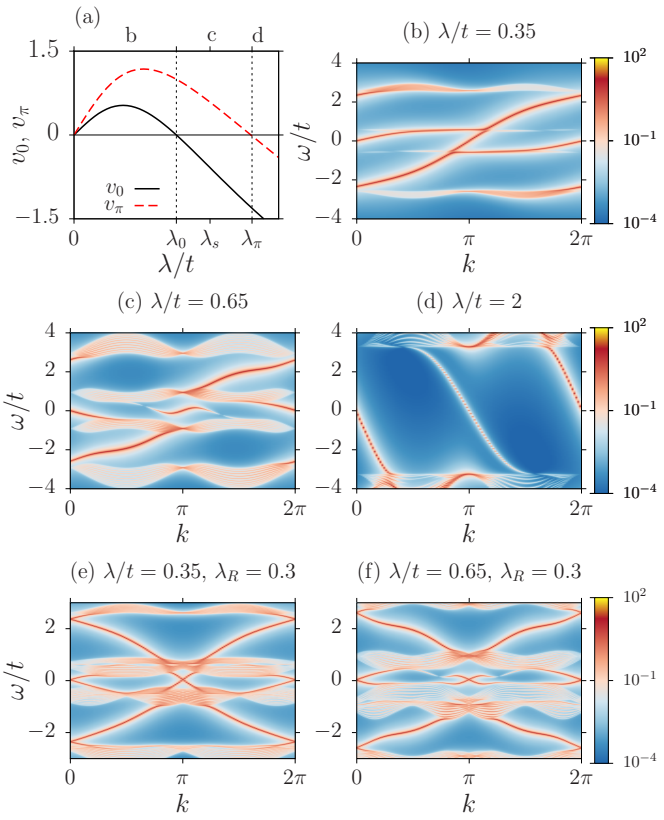

FIG. 5. (Color online) (a) The Fermi velocity v_0 (v_π) changes sign at λ_0 (λ_π) so that for $\lambda_0 < \lambda < \lambda_\pi$, the $(0, \sigma)$ and (π, σ) edge modes have opposite chirality. λ_s defines a symmetric point where $v_0 = -v_\pi$ holds. (b)–(d) Single-particle spectral function $A^\uparrow(k, \omega)$ along the edge. (e),(f) Spin-averaged single-particle spectral function $A(k, \omega) = \sum_\sigma A^\sigma(k, \omega)/2$ along the edge. Here, $\lambda_R = 0$ in (a)–(d), and $\lambda_R/t = 0.3$ in (e),(f).

$\lambda_0 < \lambda/t < \lambda_\pi$ which are gapped out by any finite Rashba coupling. Then, the effective Hamiltonian can be written in terms of right (left) moving fields $R_1(x)$ [$L_1(x)$] at the Fermi wave vector $k_F^{(1)} = 0$ and right (left) moving fields $R_2(x)$ [$L_2(x)$] at $k_F^{(2)} = \pi$:

$$\mathcal{H} = \int \mathrm{d}x \mathbf{\Psi}^\dagger(x) H_{\mathrm{edge}}(-i\partial_x) \mathbf{\Psi}(x) \,, \tag{24}$$

where $\mathbf{\Psi}^\dagger(x) = (R_1^\dagger(x), L_1^\dagger(x), R_2^\dagger(x), L_2^\dagger(x))$. The chiral fields have the anticommutation relations

$$\begin{aligned} \{R_i(x), R_j^\dagger(x')\} &= \{L_i(x), L_j^\dagger(x')\} = \delta_{ij}\delta(x - x') \,, \\ \{R_i(x), L_j^\dagger(x')\} &= \{L_i(x), R_j^\dagger(x')\} = 0 \,. \end{aligned} \tag{25}$$

In the $U(1)$ spin symmetric case, we have

$$H_{\mathrm{edge}}(-i\partial_x) = -i\partial_x \,\mathrm{diag}(v_1, v_2) \otimes \sigma_z \,. \tag{26}$$

Hamiltonian (24) will be the starting point for the bosonization analysis in Sec. VII.

A. Effective low-energy model

The edge of a two-dimensional bulk has two time-reversal invariant momenta, $k = 0$ and $k = \pi$, and therefore several possibilities exist to have two pairs of helical edge states: (i) both Kramers doublets cross at $k = 0$ (or $k = \pi$), (ii) one Kramers doublet crosses at $k = 0$ while the other crosses at $k = \pi$, and (iii) each Kramers doublet has one branch at $-k$ (or $\pi - k$) and its time-reversed branch at $+k$ (or $\pi + k$). In cases (i) and (iii), degenerate states which are not Kramers partners exist at the same momentum and can be mixed by single-particle backscattering. The edge states (i) and (iii) are therefore unstable at the single-particle level. In contrast, the edge states (ii) are stable at the single-particle level if translation symmetry is preserved at the edge, thereby forbidding scattering between states at $k = 0$ and $k = \pi$.

The metallic edge modes of Eq. (7) are an instance of case (ii). Given time-reversal symmetry and no interactions, the edge states remain gapless even in the generic case without $U(1)$ spin symmetry as long as translation symmetry and hence the momentum k along the edge is preserved. On the other hand, the states acquire a gap when time-reversal symmetry is broken. This is the case in the presence of, for example, a Zeeman term that also breaks the $U(1)$ spin symmetry.

To illustrate this point, we consider the most general time-reversal symmetric formulation of the model (24) in momentum space. Let $R_i^\dagger(p)$ $[L_i^\dagger(p)]$ create an electron with velocity v_i $[-v_i]$ (where $v_1 \equiv v_0$ and $v_2 \equiv v_\pi$) and momentum $k = p + (i-1)\pi$. Then, Eq. (24) reads

$$\mathcal{H} = \sum_p \mathbf{\Psi}^\dagger(p) H_{\rm edge}(p) \mathbf{\Psi}(p) \,, \tag{27}$$

where $\mathbf{\Psi}^\dagger(p) = (R_1^\dagger(p), L_1^\dagger(p), R_2^\dagger(p), L_2^\dagger(p))$ and

$$H_{\rm edge}(p) = H_{\rm SO}(p) + H_{\rm S} \,, \tag{28}$$

where $H_{\rm SO}(p)$ is a general spin-orbit term and $H_{\rm S}$ a single-particle scattering term. Time-reversal symmetry is preserved when $\Theta H_{\rm edge}(p)\Theta^{-1} = H_{\rm edge}(-p)$, where $\Theta = \Gamma^3\Gamma^5 K$. Here, K denotes complex conjugation and the Γ matrices were defined in Sec. II.

The spin-orbit coupling

$$H_{\rm SO} = p \begin{pmatrix} v_1 \boldsymbol{\sigma}\cdot\boldsymbol{e}_1 & 0 \\ 0 & v_2 \boldsymbol{\sigma}\cdot\boldsymbol{e}_2 \end{pmatrix} = H_{U(1)}(p) + H_{\rm R}(p) \tag{29}$$

can be split into a $U(1)$ spin-symmetric term, $H_{U(1)}(p)$, and a Rashba term, $H_{\rm R}(p)$. The (not necessarily equal) spin quantization axes are labeled by real unit vectors $\boldsymbol{e}_i$. Choosing $\boldsymbol{e}_i$ to point along the z-axis one may write the $U(1)$ spin symmetric part as

$$H_{U(1)}(p) = p \begin{pmatrix} v_1 \sigma_z e_1^z & 0 \\ 0 & v_2 \sigma_z e_2^z \end{pmatrix} = p\left(v_+ \Gamma^{15} + v_- \Gamma^{34}\right) \,, \tag{30}$$

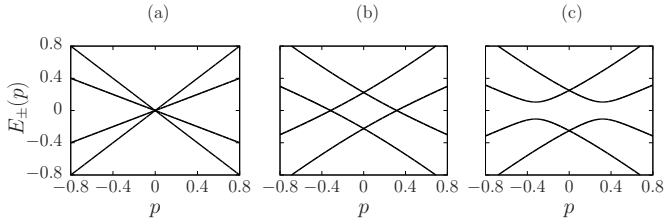

FIG. 6. Spectrum $E_\pm(p)$ of the effective model (28), with $v_1 = 1$, $v_2 = 0.5$, and $\boldsymbol{e}_1 = \boldsymbol{e}_2 = \boldsymbol{e}_z$. (a) Both translation symmetry and $U(1)$ spin symmetry are preserved ($\alpha_i = 0$). (b) Translation symmetry is broken, but $U(1)$ spin symmetry is preserved ($\alpha_1 = 0.2$, $\alpha_5 = 0.1$, $\alpha_3 = \alpha_4 = 0$). (c) Both translation symmetry and $U(1)$ spin symmetry are broken ($\alpha_1 = 0.2$, $\alpha_5 = 0.1$, $\alpha_3 = 0.1$, $\alpha_4 = 0.05$).

where $v_\pm = (v_1 e_1^z \pm v_2 e_2^z)/2$. Note that the generator of the $U(1)$ spin symmetry is $\Gamma^{34} = \mathbb{1} \otimes \sigma_z$.

One way to break the $U(1)$ spin symmetry is to include the Rashba term $H_{\rm R}(p)$ by setting $\boldsymbol{e}_1 \neq \boldsymbol{e}_2$. This can be accomplished by choosing, for example, $\boldsymbol{e}_1 = (0, 0, e_1^z)^T$ and $\boldsymbol{e}_2 = (e_2^x, e_2^y, e_2^z)^T$, leading to

$$\begin{aligned} H_{\rm R}(p) &= p v_2 \begin{pmatrix} 0 & 0 \\ 0 & \sigma_x e_2^x + \sigma_y e_2^y \end{pmatrix} \\ &= \frac{p v_2}{2}\left[(\Gamma^{45} - \Gamma^{13}) e_2^x - (\Gamma^{35} + \Gamma^{14}) e_2^y\right] \,. \end{aligned} \tag{31}$$

$H_{\rm S}$ breaks the translation symmetry of the bulk model in the sense that it allows single-particle scattering between the $i = 1$ and $i = 2$ branches of the low-energy model. Its general, time-reversal symmetric form is

$$\begin{aligned} H_{\rm S} &= \begin{pmatrix} 0 & h_{\rm S} \\ h_{\rm S}^\star & 0 \end{pmatrix} = \alpha_1\Gamma^1 + \alpha_3\Gamma^3 + \alpha_4\Gamma^4 + \alpha_5\Gamma^5 \\ &= H_{{\rm S},U(1)} + H_{{\rm S}'} \,, \end{aligned} \tag{32}$$

where $h_{\rm S}$ denotes the corresponding complex 2×2 matrix and $\alpha_i \in \mathbb{R}$. Note that $H_{\rm S}$ generally breaks the $U(1)$ spin symmetry since $[H_{\rm S}, \Gamma^{34}] = 2i(\alpha_4\Gamma^3 - \alpha_3\Gamma^4)$. Therefore, we write it as the sum of a symmetry-preserving term, $H_{{\rm S},U(1)} = \alpha_1\Gamma^1 + \alpha_5\Gamma^5$, and a symmetry-breaking term, $H_{{\rm S}'} = \alpha_3\Gamma^3 + \alpha_4\Gamma^4$.

We consider the following three cases: (a) unbroken translation symmetry and unbroken $U(1)$ spin symmetry, (b) broken translation symmetry but unbroken spin symmetry, and (c) broken translation symmetry and broken spin symmetry.

In case (a), we have $H_{\rm S} = 0$, and $U(1)$ spin symmetry amounts to $\boldsymbol{e}_1 = \boldsymbol{e}_2$. This implies $H_{\rm R}(p) = 0$, so that

$$H_{\rm edge}^{(a)}(p) = H_{U(1)}(p) \,. \tag{33}$$

The spectrum of $H_{\rm edge}^{(a)}(p)$ is gapless, as shown in Fig. 6(a).

In case (b), we have

$$H_{\rm edge}^{(b)}(p) = H_{U(1)}(p) + H_{{\rm S},U(1)} \,, \tag{34}$$

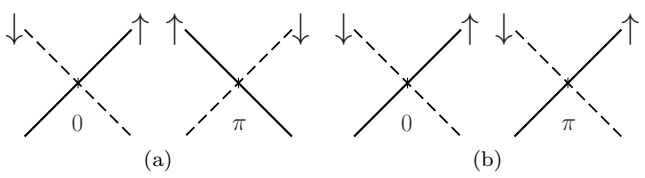

FIG. 7. The $(0,\sigma)$ and (π,σ) edge modes at (a) $\lambda/t = \lambda_s$ where $v_{0,\sigma} = -v_{\pi,\sigma}$, (b) $\lambda/t \to \infty$ where $v_{0,\sigma} = v_{\pi,\sigma}$.

and the spectrum, shown in Fig. 6(b), has two cones centered at $p_0 = \pm\sqrt{(\alpha_1^2+\alpha_5^2)/(v_+^2 - v_-^2)}$, with the linearized dispersion

$$E_\pm(p) = \pm\frac{v_+^2 - v_-^2}{v_+}(p \pm p_0) + \mathcal{O}(p^2) \,. \tag{35}$$

This illustrates that, as long as spin is conserved, the breaking of translation symmetry does not gap out the edge states.

Finally, case (c) can be realized by adding the Rashba term (31) to Eq. (34) or, alternatively, by considering

$$H^{(c)}_{\rm edge}(p) = H_{U(1)}(p) + H_{\rm S} \,, \tag{36}$$

where $\alpha_i \neq 0$. The resulting spectrum is gapped, see Fig. 6(c).

Returning to the original πKM model (7), we expect the combination of disorder (which breaks translation symmetry) and Rashba spin-orbit coupling to open a gap in the edge states. We have measured the spin polarization carried by the helical edge modes as a function of disorder strength and using twisted boundary conditions [41]. Although the pair of Kramers doublets is in general not protected from localization by disorder, the spin polarization takes on finite values up to sizable disorder strengths. We attribute this finding to strong finite-size effects. The question of edge state destruction by disorder deserves further investigation.

B. Low-energy spin symmetries at $\lambda/t = \lambda_s$ and for $\lambda/t \to \infty$

In the following, we focus on two values of the intrinsic spin-orbit coupling, $\lambda/t = \lambda_s$ and $\lambda/t \to \infty$, where the velocities of the $(0,\sigma)$ and the (π,σ) modes obey $v_{0,\sigma} = -v_{\pi,\sigma}$ and $v_{0,\sigma} = v_{\pi,\sigma}$, respectively (see Fig. 7). The corresponding low-energy Hamiltonians are

$$H^s_{\rm edge}(-i\partial_x) = -i\partial_x v \begin{pmatrix} \sigma_z & 0 \\ 0 & -\sigma_z \end{pmatrix} = -i\partial_x v \Gamma^{15} \,, \tag{37}$$

where $\mathbf{\Psi}_s^\dagger(x) = (R_1^\dagger(x), L_1^\dagger(x), L_2^\dagger(x), R_2^\dagger(x))$, and

$$H^\infty_{\rm edge}(-i\partial_x) = -i\partial_x v \begin{pmatrix} \sigma_z & 0 \\ 0 & \sigma_z \end{pmatrix} = -i\partial_x v \Gamma^{34} \,, \tag{38}$$

where $\mathbf{\Psi}_\infty^\dagger(x) = (R_1^\dagger(x), L_1^\dagger(x), R_2^\dagger(x), L_2^\dagger(x))$. While the $SU(2)$ spin symmetry is obviously broken, we show in the following that a chiral $SU(2)$ symmetry exists for $\lambda/t = \lambda_s$.

The electron annihilation operator $\hat{c}_\sigma(x)$ can be written in terms of the fields $R_i(x)$ and $L_i(x)$ [42],

$$\begin{aligned} \hat{c}_\uparrow(x) &= \left[R_1(x)e^{-ik_{\rm F}^{(1)}x} + Y_2(x)e^{-ik_{\rm F}^{(2)}x}\right]/\sqrt{2} \,, \\ \hat{c}_\downarrow(x) &= \left[L_1(x)e^{-ik_{\rm F}^{(1)}x} + \bar{Y}_2(x)e^{-ik_{\rm F}^{(2)}x}\right]/\sqrt{2} \,, \end{aligned} \tag{39}$$

where $k_{\rm F}^{(1)} = 0$, $k_{\rm F}^{(2)} = \pi$. For $\lambda/t = \lambda_s$, the $i = 1$ and $i = 2$ modes have opposite helicity, so $Y_2(x) = L_2(x)$ and $\bar{Y}_2(x) = R_2(x)$. For $\lambda/t \to \infty$, we have $Y_2(x) = R_2(x)$ and $\bar{Y}_2(x) = L_2(x)$. The fermionic anticommutation relations follow from Eq. (25). The spin operators can be expressed for both cases as

$$\begin{aligned} \hat{S}^a(x) &= \frac{1}{2}\sum_{\sigma,\sigma'} \hat{c}^\dagger_\sigma(x)\sigma^a_{\sigma,\sigma'}\hat{c}_{\sigma'}(x) \\ &= \frac{1}{4}\sum_{\sigma,\sigma'} \Psi^\dagger_\sigma(x) s^a_{\sigma,\sigma'}\Psi_{\sigma'}(x) \,, \end{aligned} \tag{40}$$

with the constraint of single occupancy, $\hat{c}^\dagger_\uparrow(x)\hat{c}_\uparrow(x) + \hat{c}^\dagger_\downarrow(x)\hat{c}_\downarrow(x) = 1$. The matrices s^a are given by

$$\begin{aligned} s^x &= \mathbb{1}\otimes\sigma_x + (\sigma_x\otimes\sigma_x)\, e^{i\pi x} = \Gamma^{45} - \Gamma^{23}e^{i\pi x} \,, \\ s^y &= \mathbb{1}\otimes\sigma_y + (\sigma_x\otimes\sigma_y)\, e^{i\pi x} = -\Gamma^{35} - \Gamma^{24}e^{i\pi x} \,, \\ s^z &= \mathbb{1}\otimes\sigma_z + (\sigma_x\otimes\sigma_z)\, e^{i\pi x} = \Gamma^{34} - \Gamma^{25}e^{i\pi x} \,. \end{aligned} \tag{41}$$

They have the commutation relation $[s^a/4, s^b/4] = i\epsilon^{abc}(s^c/4)$.

Apart from the spin operators, Eq. (40), there are three additional operators which have the commutation relations of the $su(2)$ Lie algebra. These operators are represented by the matrices

$$\Sigma_x \equiv \Gamma^{23} \,, \quad \Sigma_y \equiv \Gamma^{24} \,, \quad \Sigma_z \equiv \Gamma^{34} \,, \tag{42}$$

which appear in Eq. (41) and satisfy $[\Sigma_a/2, \Sigma_b/2] = i\epsilon^{abc}(\Sigma_c/2)$. They are related to the additional chiral degree of freedom which is introduced by the edge mode 'orbitals' taking the values $i = 1, 2$. For $\lambda/t = \lambda_s$, all three generators Σ_a are symmetries of the low-energy Hamiltonian (37), i.e., $[H^s_{\rm edge}, \Sigma_a] = 0$, whereas for $\lambda/t \to \infty$, this is only true for Σ_z. Therefore, and apart from the spin symmetry, a chiral $SU(2)$ symmetry is present for $\lambda/t = \lambda_s$ which turns into a chiral $U(1)$ symmetry for $\lambda/t \to \infty$.

We define a rotation by $\pi/2$, described by

$$U_a = \exp\left[-i(\pi/4)\Sigma_a\right] = (\mathbb{1} - i\Sigma_a)/\sqrt{2} \,. \tag{43}$$

Then, $U_a^\dagger \hat{S}^b(x) U_a = M_{ab}$ is the rotation by $\pi/2$ of the spin component $\hat{S}^b(x)$ around the $\boldsymbol{e}_a$ axis, where

$$M = \begin{pmatrix} \hat{S}^x(x) & e^{i\pi x}\hat{S}^z(x) & -e^{i\pi x}\hat{S}^y(x) \\ -e^{i\pi x}\hat{S}^z(x) & \hat{S}^y(x) & e^{i\pi x}\hat{S}^x(x) \\ -\hat{S}^y(x) & \hat{S}^x(x) & \hat{S}^z(x) \end{pmatrix} \,. \tag{44}$$

In particular, we obtain the relations

$$\begin{aligned} U_x^\dagger \hat{S}^z(x) U_x &= -e^{i\pi x}\hat{S}^y(x) \,, \\ U_y^\dagger \hat{S}^z(x) U_y &= e^{i\pi x}\hat{S}^x(x) \,, \\ U_z^\dagger \hat{S}^y(x) U_z &= \hat{S}^x(x) \,. \end{aligned} \tag{45}$$

We now consider the static spin structure factor

$$S^a(q) = \frac{1}{\sqrt{N}} \sum_x e^{-iqx} \langle \hat{S}^a(x) \hat{S}^a(0) \rangle \,, \tag{46}$$

where the expectation value is defined with respect to the effective Hamiltonian (24). Using the symmetry relations (45) we get

$$\begin{aligned} &S^z(q) = S^x(q+\pi) \quad \text{for } \lambda/t = \lambda_s \,, \\ &S^x(q) = S^y(q) \qquad\quad \text{for } \lambda/t = \lambda_s \text{ and } \lambda/t \to \infty \,. \end{aligned} \tag{47}$$

Equation (47) relates the longitudinal and transverse components of the spin-spin correlation functions. In Sec. VIII, we numerically show that this low-energy symmetry is preserved in the presence of interactions. It is therefore an emergent symmetry of the interacting πKMH model (8). However, because the chiral spins [Eq. (42)] do not commute with the Rashba term [e.g., Eq. (31)], this symmetry hinges on $U(1)$ spin symmetry.

VII. BOSONIZATION FOR THE EDGE STATES

At low energies, the edge states of the πKMH model (8) can be described in terms of a two-component [43–46] Tomonaga-Luttinger liquid [42, 47]. The Tomonaga-Luttinger liquid is the stable low-energy fixed point of gapless interacting systems in one dimension [48]. We consider the free Hamiltonian with two left and two right movers, forward scattering within the $i = 1$ and $i = 2$ branches (intra-forward scattering of strength $g_f^{(i)}$), and between the branches (inter-forward scattering of strength g_f'). We focus on the case of two pairs of edge modes crossing at $k = 0$ and $k = \pi$, respectively, since only those are protected by time-reversal symmetry. In the following, we show that at half filling umklapp scattering between the edge modes is a relevant perturbation in the sense of the renormalization group (RG). It can drive the model away from the Luttinger liquid fixed point and open gaps in the low-energy spectrum.

We consider the following kinetic and interaction terms,

$$\begin{aligned} \mathcal{H} = \sum_{i=1}^{2} \Big[v_i \int \mathrm{d}x \left(L_i^\dagger (i\partial_x) L_i + R_i^\dagger (-i\partial_x) R_i \right) \\ + g_f^{(i)} \int \mathrm{d}x \, \rho_i^2 \Big] + g_f' \int \mathrm{d}x \, \rho_1 \rho_2 \,, \end{aligned} \tag{48}$$

where L_i (R_i) are the left (right) moving fields, and $\rho_i = R_i^\dagger R_i + L_i^\dagger L_i$ is the electronic density.

To bosonize the above Hamiltonian (48), we introduce the bosonic fields $\phi_i(x)$, with $\partial_x \phi_i = \pi \rho_i$, and $\Pi_i = R_i^\dagger R_i - L_i^\dagger L_i$, where $[\phi_i(x), \Pi_{i'}(x'] = i\delta_{i,i'}\delta(x-x')$. We then have

$$\begin{aligned} \mathcal{H} &= \frac{1}{2\pi} \int \mathrm{d}x \sum_{i=1}^{2} \left[v_i \left(\pi \Pi_i\right)^2 + v_i K_i^{-2} \left(\partial_x \phi_i\right)^2 \right] \\ &\quad + \frac{g_f'}{\pi^2} \int \mathrm{d}x \, \partial_x \phi_1 \partial_x \phi_2 \\ &= \frac{1}{2\pi} \int \mathrm{d}x \left[\pi^2 \Pi^T M \Pi + \left(\partial_x \phi\right)^T N \partial_x \phi \right] \,, \end{aligned} \tag{49}$$

where $K_i = (1 + 2g_f^{(i)}/\pi v_i)^{-1/2}$ is a dimensionless parameter. In the last line, we defined $\Pi = (\Pi_1, \Pi_2)^T$, $\phi = (\phi_1, \phi_2)^T$, and

$$M = \begin{pmatrix} v_1 & 0 \\ 0 & v_2 \end{pmatrix} , \; N = \frac{1}{\pi} \begin{pmatrix} \pi v_1 + 2g_f^{(1)} & g_f' \\ g_f' & \pi v_2 + 2g_f^{(2)} \end{pmatrix} , \tag{50}$$

using the notation of Orignac *et al.* [44, 49]. The off-diagonal elements in M are zero, since there is no single-particle scattering from the $i = 1$ to the $i = 2$ cone. Hamiltonian (49) is decoupled by rescaling the fields:

$$\begin{aligned} \mathcal{H} &= \frac{1}{2\pi} \int \mathrm{d}x \left[\pi^2 \Pi'^T \Pi' + \left(\partial_x \phi'\right)^T M^{1/2} N M^{1/2} \partial_x \phi' \right] \\ &= \frac{1}{2\pi} \int \mathrm{d}x \left[\pi^2 \Pi''^T \Pi'' + \left(\partial_x \phi''\right)^T \Delta \partial_x \phi'' \right] \\ &= \frac{1}{2\pi} \int \mathrm{d}x \sum_{i=1}^{2} \Delta_{ii}^{1/2} \left[\pi^2 \widetilde{\Pi}_i^2 + \left(\partial_x \widetilde{\phi}_i\right)^2 \right] \,, \end{aligned} \tag{51}$$

where $\Pi' = M^{1/2}\Pi$, $\phi' = M^{-1/2}\phi$, $\Pi'' = S^{-1}\Pi'$, $\phi'' = S^{-1}\phi'$, $\widetilde{\Pi} = \Delta^{-1/4}\Pi''$, and $\widetilde{\phi} = \Delta^{1/4}\phi''$. Δ is a diagonal matrix and S a rotation, defined via $\Delta = S^{-1} M^{1/2} N M^{1/2} S$. Therefore, the linear transformation to the new bosonic fields $\widetilde{\Pi}$ and $\widetilde{\phi}$ is $\Pi = M^{-1/2} S \Delta^{1/4} \widetilde{\Pi} \equiv P \widetilde{\Pi}$ and $\phi = M^{1/2} S \Delta^{-1/4} \widetilde{\phi} \equiv Q \widetilde{\phi}$. The canonical commutation relations are preserved, since

$$\begin{aligned} \left[\widetilde{\phi}_i(x), \widetilde{\Pi}_{i'}(x') \right] &= \sum_{k,k'} Q_{i,k}^{-1} \left(P^{-1}\right)_{k',i'}^T \left[\phi_k(x), \Pi_{k'}(x') \right] \\ &= i\delta_{i,i'}\delta(x-x') \,. \end{aligned} \tag{52}$$

We have

$$Q = \begin{pmatrix} S_{11} v_1^{1/2} \Delta_{11}^{-1/4} & S_{12} v_1^{1/2} \Delta_{22}^{-1/4} \\ S_{21} v_2^{1/2} \Delta_{11}^{-1/4} & S_{22} v_2^{1/2} \Delta_{22}^{-1/4} \end{pmatrix} , \tag{53}$$

$$\begin{aligned} \Delta_{ii} = \frac{v_1 N_{11} + v_2 N_{22}}{2} \\ \pm \left[\left(\frac{v_1 N_{11} - v_2 N_{22}}{2} \right)^2 + v_1 v_2 N_{12}^2 \right]^{1/2} \,, \end{aligned} \tag{54}$$

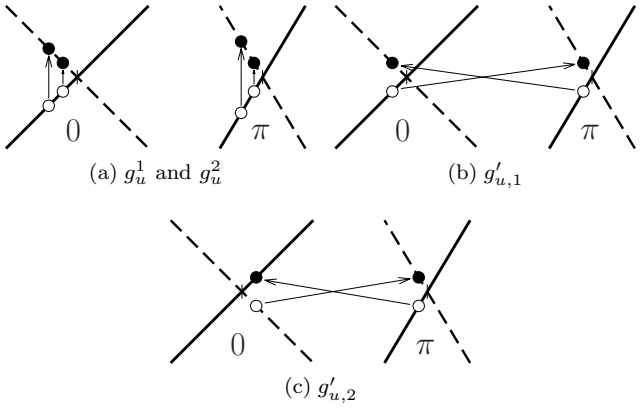

FIG. 8. The edge modes cross at $k = 0$ and $k = \pi$ with in general nonequivalent Fermi velocities v_1 and v_2. We consider the intra-umklapp scattering process (a), and the inter-umklapp scattering processes (b) and (c).

and, for $g'_f \neq 0$,

$$S = \begin{pmatrix} \frac{\mathrm{sgn}(g'_f)}{\sqrt{1+s_1}} & \frac{\mathrm{sgn}(g'_f)}{\sqrt{1+s_2}} \\ \frac{\mathrm{sgn}(\Delta_{11}-v_1N_{11})}{\sqrt{1+s_1^{-1}}} & \frac{\mathrm{sgn}(\Delta_{22}-v_1N_{11})}{\sqrt{1+s_2^{-1}}} \end{pmatrix} , \qquad (55)$$

where $s_i = (\Delta_{ii} - N_{11}v_1)^2/v_1v_2N_{12}^2$. For $g'_f = 0$, $S = \mathbb{1}$.

We consider the following interactions as perturbations to Eq. (51): intra-umklapp scattering of strength $g_u^{(i)}$ [Fig. 8(a)], inter-umklapp scattering of strength $g'_{u,1}$ [Fig. 8(b)], and inter-umklapp scattering of strength $g'_{u,2}$ [Fig. 8(c)]. These processes are described by

$$\begin{aligned} \mathcal{H}' = &\sum_{i=1}^{2} g_u^{(i)} \int \mathrm{d}x\; L_i^\dagger(x) L_i^\dagger(x+a) R_i(x) R_i(x+a) \\ &\times e^{i4k_{\mathrm{F}}^{(i)}x} \\ &+ g'_{u,1} \int \mathrm{d}x\; L_1^\dagger(x) L_2^\dagger(x) R_1(x) R_2(x)\; e^{i2(k_{\mathrm{F}}^{(1)}+k_{\mathrm{F}}^{(2)})x} \\ &+ g'_{u,2} \int \mathrm{d}x\; L_1^\dagger(x) R_2^\dagger(x) L_2(x) R_1(x)\; e^{i2(k_{\mathrm{F}}^{(1)}-k_{\mathrm{F}}^{(2)})x} \\ &+ \mathrm{H.c.} \end{aligned} \qquad (56)$$

The fermionic operators are $R_i = \exp(-i\phi_{R,i})/\sqrt{2\pi}$ and $L_i = \exp(i\phi_{L,i})/\sqrt{2\pi}$, omitting the Klein factors, and we have $\phi_i = (\phi_{R,i} + \phi_{L,i})/2$. We take $4k_{\mathrm{F}}^{(i)}x = 2(k_{\mathrm{F}}^{(1)} + k_{\mathrm{F}}^{(2)})x = 2(k_{\mathrm{F}}^{(1)} - k_{\mathrm{F}}^{(2)})x = 2\pi n$, corresponding to half-filled bands. Then,

$$\begin{aligned} \mathcal{H}' = &\sum_{i=1}^{2} \frac{g_u^{(i)}}{2\pi^2} \int \mathrm{d}x \cos\left(4\phi_i\right) + \frac{g'_{u,1}}{2\pi^2} \int \mathrm{d}x \cos\left[2\left(\phi_1+\phi_2\right)\right] \\ &+ \frac{g'_{u,2}}{2\pi^2} \int \mathrm{d}x \cos\left[2\left(\phi_1-\phi_2\right)\right] . \end{aligned} \qquad (57)$$

We now consider $\mathcal{H} + \mathcal{H}'$ and obtain the scaling dimensions $\Delta_u^{(i)}$, Δ'_{u1}, and Δ'_{u2}, of the vertex operators $\exp(i4\phi_i)$ and $\exp[i2(\phi_1 \pm \phi_2)]$ in the above scattering processes [47]:

$$\begin{aligned} \Delta_u^{(1)} &= 4\left(Q_{11}^2 + Q_{12}^2\right), \\ \Delta_u^{(2)} &= 4\left(Q_{21}^2 + Q_{22}^2\right), \\ \Delta'_{u1} &= \left(Q_{11}+Q_{21}\right)^2 + \left(Q_{12}+Q_{22}\right)^2, \\ \Delta'_{u2} &= \left(Q_{11}-Q_{21}\right)^2 + \left(Q_{12}-Q_{22}\right)^2 , \end{aligned} \qquad (58)$$

The scaling dimension Δ determines whether the respective scattering process in $\mathcal{H}'$ [Eq. (57)] is a relevant ($\Delta < 2$) or irrelevant ($\Delta > 2$) perturbation to the free bosonic Hamiltonian $\mathcal{H}$ [Eq. (51)]. For $g'_f = 0$, we have two separate Dirac cones, with $\Delta_u^{(i)} = 4v_i\Delta_{ii}^{-1/2} = 4K_i$ [see Eq. (49)]. Therefore, intra-umklapp scattering ($g_f^{(i)}$) becomes relevant when $K_i < 1/2$, reproducing the result for a one-component helical liquid [6, 7].

In the case of weak coupling ($g_f^{1,2} \ll 1$ and $g'_f \ll 1$), we come to the following conclusions: (i) Intra-umklapp scattering is RG-irrelevant, with $\Delta_u^{(1,2)} > 2$. This is similar to the case of the one-component helical liquid [6, 7]. (ii) Inter-umklapp scattering $g'_{u,1}$ is RG-relevant, with $\Delta'_{u1} < 2$. (iii) The relevance of the inter-umklapp scattering $g'_{u,2}$ is determined by the phase diagram shown in Fig. 9.

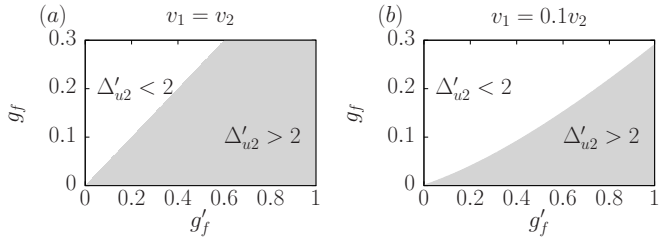

FIG. 9. Phase diagram of the inter-umklapp process $g'_{u,2}$ in the (g'_f,g_f) plane for (a) equivalent and (b) nonequivalent velocities of the edge modes. The scattering process is relevant (irrelevant) in the region where $\Delta'_{u2} < 2$ ($\Delta'_{u2} > 2$).

If the $U(1)$ spin symmetry is preserved, only one of the two inter-umklapp scattering processes $g'_{u,1}$ or $g'_{u,2}$ is allowed by symmetry, depending on the chirality of the $(0,\sigma)$ and (π,σ) modes which is determined by the intrinsic spin-orbit coupling λ. As shown in Fig. 5(a), for $\lambda/t < \lambda_0$ and $\lambda/t > \lambda_\pi$, both edge movers have the same chirality so that inter-umklapp scattering corresponds to the $g'_{u,2}$ term. In contrast, for $\lambda_0 < \lambda/t < \lambda_\pi$, the edge movers have opposite chirality and inter-umklapp scattering is given by the $g'_{u,1}$ term.

The above distinction no longer holds when the $U(1)$ spin symmetry is broken. In this case, $g'_{u,1}$ is always RG-relevant, whereas the relevance of $g'_{u,2}$ depends on the forward scattering strengths g_f and g'_f and on the edge velocities, see Fig. 9.

For $\lambda/t = \lambda_{\mathrm{s}}$ ($\lambda/t \to \infty$), our low-energy theory is similar to the fusion of two anti-parallel (parallel) helical

edge modes [43], see also Fig. 7. However, in the latter setup, the spatial overlap of the two edge wave functions can be neglected, whereas it is included in the interaction term of Eq. (48).

VIII. QUANTUM MONTE CARLO RESULTS FOR EDGE CORRELATION EFFECTS

Correlation effects on the edge states of the πKMH model can be studied numerically using the approach discussed in Sec. III. Considering a zigzag ribbon, we take into account a Hubbard interaction only at one edge, and simulate the resulting model exactly using the CT-INT quantum Monte Carlo method.

We focus on two values of the spin-orbit coupling λ/t and set the Rashba coupling to $\lambda_R/t = 0.3$. For $\lambda/t = 0.35$, the edge modes at $k = 0$ and $k = \pi$ have different velocities ($v_0 < v_\pi$), whereas at $\lambda/t = 0.65$, we have $v_0 \approx v_\pi$. As in the KMH model [32], we observe that the velocities of the edge states remain almost unchanged with respect to the noninteracting case.

We carried out simulations for a zigzag ribbon of dimensions $L_1 = 25$ (open boundary condition) and $L_2 = 16$ (periodic boundary condition), see also Fig. 4(a). For $\lambda_R = 0$, $\mu = 0$ corresponds to half filling. Although the band filling in general changes as a function of λ_R (the Rashba term breaks the particle-hole symmetry), the Kramers degenerate edge states at $k = 0, \pi$ are pinned to $\omega = \mu$. The choice $\mu = 0$ then again corresponds to half-filled Dirac cones, and allows for umklapp scattering processes. The inverse temperature was set to $\beta t = 60$.

A. Single-particle spectral function

Using CT-INT in combination with the stochastic maximum entropy method [50], we calculate the spin-averaged spectral function at the edge,

$$A(k,\omega) = \frac{1}{2}\sum_\sigma A^\sigma(k,\omega)\,, \qquad (59)$$
$$A^\sigma(k,\omega) = -\frac{1}{\pi}\mathrm{Im}\, G^\sigma(k,\omega)\,,$$

where $G^\sigma(k,\omega)$ is the interacting single-particle Green function, and k is the momentum along the edge.

As shown in Fig. 10(a), for $U/t = 2$, the numerical results suggest the existence of gapless edge states. In contrast, for a stronger interaction $U/t = 5$, a gap is clearly visible both at $k = 0$ and $k = \pi$. While the bosonization analysis in Sec. VII predicts a gap as a result of relevant umklapp scattering for any $U > 0$, the size of the gap depends exponentially on U/t. The apparent absence of a gap in Fig. 10(a) can therefore be attributed to the small system size used ($L_2 = 16$).

Figure 10(c) shows the spectral function (59) for $\lambda/t = 0.35$, where $v_0 < v_\pi$. Compared to the case of $\lambda/t = 0.65$ [Fig. 10(b)] where $v_0 \approx v_\pi$, the gap in the edge states is much smaller. We expect this dependence on the Fermi velocities to also emerge from the bosonization in the form of a velocity-dependent prefactor that determines the energy scale of the gap [51].

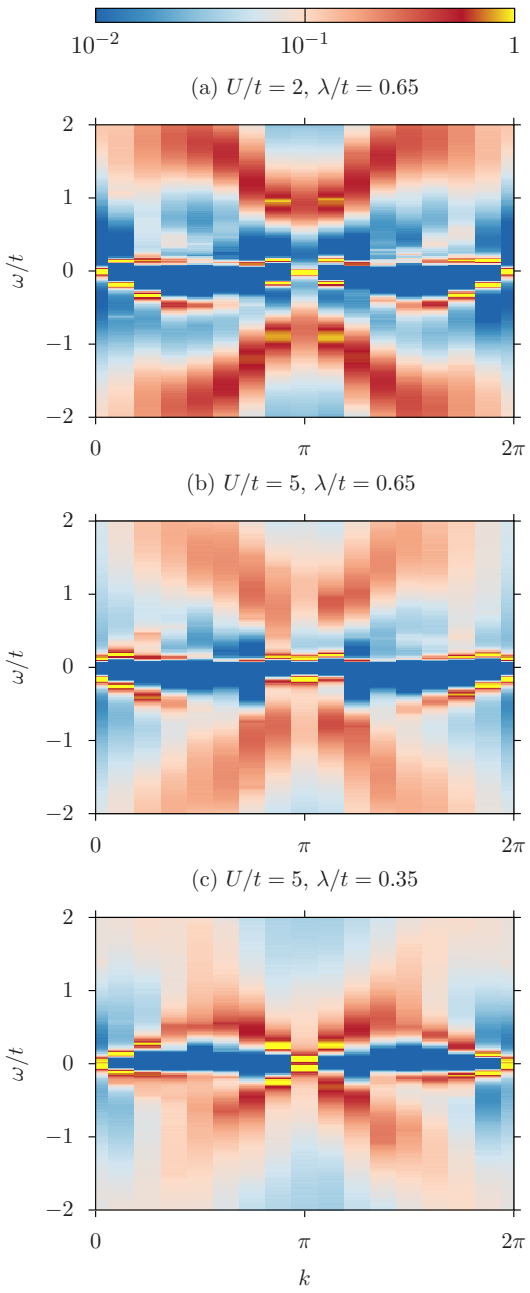

FIG. 10. (Color online) Spin-averaged single-particle spectral function $A(k,\omega)$ [Eq. (59)] from CT-INT simulations. (a) Weak coupling $U/t = 2$, (b),(c) strong coupling $U/t = 5$. Here, $\lambda_R/t = 0.3$.

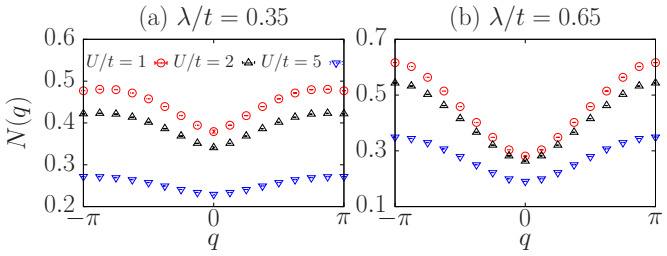

FIG. 11. (Color online) Charge structure factor $N(q)$ [Eq. (60)] from CT-INT simulations for (a) $\lambda/t = 0.35$ and (b) $\lambda/t = 0.65$. Here, $\lambda_R/t = 0.3$.

B. Charge and spin structure factors

We consider the charge structure factor

$$N(q) = \frac{1}{\sqrt{N}} \sum_x e^{-iqx} \left[\langle \hat{n}(x)\hat{n}(0)\rangle - \langle \hat{n}(x)\rangle\langle \hat{n}(0)\rangle\right] , \tag{60}$$

where x is the position along the edge. Figure 11(b) shows results for different values of U/t, $\lambda/t = 0.65$, and $\lambda_R/t = 0.3$. For a weak interaction, $U/t = 1$, $N(q)$ exhibits cusps at $q = 0$ and $q = \pi$ that indicate a power-law decay of the real-space charge correlations. Upon increasing U/t, the cusps becomes less pronounced, which suggests a suppression of charge correlations by the interaction. This is in accordance with the existence of a gap in the single-particle spectral function [Fig. 10(b)]. A suppression of charge correlations is also observed for $\lambda = 0.35$, see Fig. 11(a).

The spin structure factors ($a = x, z$)

$$S^a(q) = \frac{1}{\sqrt{N}} \sum_x e^{-iqx} \langle \hat{S}^a(x)\hat{S}^a(0)\rangle \tag{61}$$

are shown in Fig. 12. For $\lambda/t = 0.65$ and $U/t = 2$, $S^x(q)$ has cusps at $q = 0$ and $q = \pi$ [Fig. 12(c)], and varies almost linearly in between. With increasing U/t [$U/t = 5$ in Fig. 12(d)], correlations with $q = 0$ become much stronger. Whereas $q = 0$ spin correlations dominate the x component of spin, the structure factor $S^z(q)$ in Fig. 12(d) indicates equally strong correlations with $q = \pi$ for the z component. The resulting spin order resembles that of a canted antiferromagnet. Qualitatively similar results, although with a less pronounced increase of spin correlations between $U/t = 2$ and $U/t = 5$, are also observed for $\lambda/t = 0.35$, as shown in Figs. 12(a),(b).

Despite a small but nonzero Rashba coupling, the results in Figs. 12(c) and (d) reveal the symmetry relation $S^z(q) = S^x(q + \pi)$ which roots in the chiral $SU(2)$ symmetry of the corresponding low-energy Hamiltonian (see Sec. VI B). Our quantum Monte Carlo results show that this symmetry survives even in the presence of strong correlations. The results in Fig. 12 are almost identical to the case with $\lambda_R = 0$ (not shown), suggesting that the

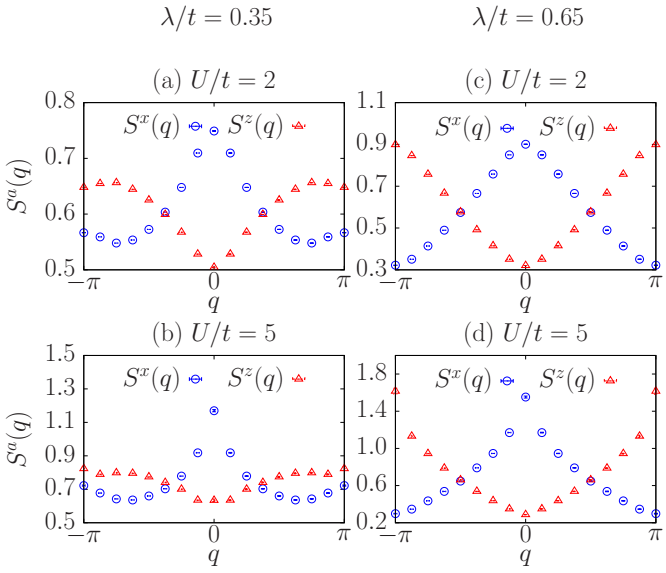

FIG. 12. (Color online) Spin structure factors $S^x(q)$ and $S^z(q)$ [Eq. (61)] from CT-INT simulations for $\lambda/t = 0.35$ [(a),(b)] and $\lambda/t = 0.65$ [(c),(d)]. Here, $\lambda_R/t = 0.3$.

Rashba term breaks the chiral symmetry only weakly. On the other hand, the symmetry is clearly absent for $\lambda/t = 0.35$ [Figs. 12(a),(b)].

C. Effective spin model for $\lambda/t = \lambda_s$

For strong interactions U/t, there exist no low-energy charge fluctuations at the edge, allowing for a description in terms of a spin model. We consider the case of (nearly) equal velocities, $\lambda/t = 0.65$, and make an ansatz in the form of a Heisenberg model with nearest-neighbor interactions,

$$\begin{aligned}\mathcal{H}_{\text{spin}} &= \sum_i \left(J_x S_i^x S_{i+1}^x + J_y S_i^y S_{i+1}^y + J_z S_i^z S_{i+1}^z\right) \\ &= J \sum_i \left(S_i^x S_{i+1}^x + S_i^y S_{i+1}^y - S_i^z S_{i+1}^z\right) . \end{aligned} \tag{62}$$

In the second line, the coupling constants J_a have been fixed by imposing the invariance under the rotations given in Eq. (43), $[H^s_{\text{spin}}, U_a] = 0$, and using the relations $U_a^\dagger \hat{S}^b(x) U_a = M_{ab}$ [cf. Eq. (44)]. Hamiltonian (62) corresponds to the XXZ Heisenberg model, tuned to the ferromagnetic isotropic point that separates the Ising phase from the Luttinger liquid phase via a first order transition. In both cases, one expects strong spin correlations, as observed in Fig. 12(d) [52].

IX. CONCLUSIONS

In this paper, we introduced the πKM model, corresponding to the Kane-Mele model on a honeycomb lat-

tice with a magnetic flux of $\pm\pi$ through each hexagon. The flux insertion doubles the size of the unit cell, and leads to a four-band model for each spin sector. For one spin direction, the band structure has four Dirac points which acquire a gap for nonzero spin-orbit coupling λ. At half filling, the spinless model has a Chern insulating ground state with Chern number 2 or -2, depending on the spin-orbit coupling. The transition between these states occurs via a phase transition at $\lambda/t = 1/2$, and the band structure features a quadratic crossing at the critical point. The spinful πKM model is trivial in the Z_2 classification, with an even number of Kramers doublets. If translation symmetry at the edge is unbroken, the helical edge states are stable at the single-particle level even in the presence of a Rashba coupling that breaks the $U(1)$ spin symmetry. The $U(1)$ spin symmetric low-energy model of the edge states has a chiral symmetry when the edge state velocities have equal magnitude and either the same or opposite sign. This chiral symmetry is shown to survive even in the presence of interactions.

Regarding the effect of electronic correlations in the bulk, the combination of mean-field calculations and quantum Monte Carlo simulations suggest the existence of a quantum phase transition to a state with long-range, antiferromagnetic order, similar to the Kane-Mele-Hubbard model. The critical value of the interaction depends on the spin-orbit coupling. At $\lambda/t = 1/2$, where the quadratic band crossing occurs, a weak-coupling Stoner instability exists.

We studied the correlation effects on the edge states in the paramagnetic bulk phase. At half filling, the bosonization analysis predicts the opening of a gap in the edge states as a result of umklapp scattering for any nonzero interaction. For strong coupling, we were able to confirm this prediction using quantum Monte Carlo simulations. Umklapp processes are only effective at commensurate filling and therefore can be eliminated by doping away from half filling. In this case, we expect the interacting model to have stable edge modes, provided translation symmetry is not broken. At large U/t, the emergent chiral symmetry can be used to derive an effective spin model of the XXZ Heisenberg type.

Our model may be regarded as a two-dimensional counterpart of TCIs. Whereas the gapless edge states of the latter are protected by crystal symmetries of the two-dimensional surface, the edge states in the πKM model are protected (at the single-particle level, or away from half filling) by translation symmetry. TCIs have an even number of surface Dirac cones which are related by a crystal symmetry. The cones can be displaced in momentum space without breaking time-reversal symmetry by applying inhomogeneous strain [53]. This is in contrast to topological insulators with an odd number of Dirac points where at least one Kramers doublet is pinned at a time-reversal invariant momentum. In TCIs, umklapp scattering processes can be avoided either by doping away from half filling or by moving the Dirac points. In our model, the edge modes have in general unequal velocities and cannot be mapped onto each other by symmetry. The Dirac points are pinned at the time-reversal invariant momenta, and subject to umklapp scattering at half filling.

Finally, the πKM model may be experimentally realized in ultracold atomic gases by using optical flux lattices to create periodic magnetic flux densities [54–58].

ACKNOWLEDGMENTS

We thank F. Crepin and B. Trauzettel for helpful discussions. We acknowledge computing time granted by the Jülich Supercomputing Centre (JUROPA), and the Leibniz Supercomputing Centre (SuperMUC). This work was supported by the DFG grants Nos. AS120/10-1 and Ho 4489/2-1 (FOR1807).

* martin.bercx@physik.uni-wuerzburg.de

[1] C. L. Kane and E. J. Mele, Phys. Rev. Lett. **95**, 146802 (2005).
[2] C. L. Kane and E. J. Mele, Phys. Rev. Lett. **95**, 226801 (2005).
[3] B. A. Bernevig, T. L. Hughes, and S.-C. Zhang, Science **314**, 1757 (2006).
[4] M. König, S. Wiedmann, C. Brüne, A. Roth, H. Buhmann, L. W. Molenkamp, X.-L. Qi, and S.-C. Zhang, Science **318**, 766 (2007).
[5] A. P. Schnyder, S. Ryu, A. Furusaki, and A. W. W. Ludwig, Phys. Rev. B **78**, 195125 (2008).
[6] C. Wu, B. A. Bernevig, and S.-C. Zhang, Phys. Rev. Lett. **96**, 106401 (2006).
[7] C. Xu and J. E. Moore, Phys. Rev. B **73**, 045322 (2006).
[8] L. Fu, Phys. Rev. Lett. **106**, 106802 (2011).
[9] T. H. Hsieh, H. Lin, J. Liu, W. Duan, A. Bansil, and L. Fu, Nat. Commun. **3**, 982 (2012).
[10] R. Slager, A. Mesaros, V. Juricic, and J. Zaanen, Nat. Phys. **9**, 98 (2013).
[11] Y. Tanaka, Z. Ren, T. Sato, K. Nakayama, S. Souma, T. Takahashi, K. Segawa, and Y. Ando, Nat. Phys. **8**, 800 (2012).
[12] P. Dziawa, B. Kowalski, K. Dybko, R. Buczko, A. Szczerbakow, M. Szot, E. Lusakowska, T. Balasubramanian, B. Wojek, M. Berntsen, O. Tjernberg, and T. Story, Nat. Mater. **11**, 1023 (2012).
[13] S. Xu, C. Liu, N. Alidoust, M. Neupane, D. Qian, I. Belopolski, J. Denlinger, Y. Wang, H. Lin, L. Wray, G. Landolt, B. Slomski, J. Dil, A. Marcinkova, E. Morosan, Q. Gibson, R. Sankar, F. Chou, R. Cava, A. Bansil, and M. Hasan, Nat. Commun. **3**, 1192 (2012).
[14] Y. Ran, A. Vishwanath, and D.-H. Lee, Phys. Rev. Lett. **101**, 086801 (2008).
[15] X.-L. Qi and S.-C. Zhang, Phys. Rev. Lett. **101**, 086802 (2008).

[16] V. Juricic, A. Mesaros, R.-J. Slager, and J. Zaanen, Phys. Rev. Lett. **108**, 106403 (2012).
[17] F. F. Assaad, M. Bercx, and M. Hohenadler, Phys. Rev. X **3**, 011015 (2013).
[18] Y.-J. Wu, J. He, and S.-P. Kou, EPL **105**, 47002 (2014).
[19] C. Weeks and M. Franz, Phys. Rev. B **81**, 085105 (2010).
[20] Y. Jia, H. Guo, Z. Chen, S.-Q. Shen, and S. Feng, Phys. Rev. B **88**, 075101 (2013).
[21] M. Kindermann, arXiv:1309.1667 (2013).
[22] F. D. M. Haldane, Phys. Rev. Lett. **61**, 2015 (1988).
[23] A. Kitaev, Annals of Physics **321**, 2 (2006).
[24] V. Lahtinen, New Journal of Physics **13**, 075009 (2011).
[25] V. Lahtinen, A. W. W. Ludwig, J. K. Pachos, and S. Trebst, Phys. Rev. B **86**, 075115 (2012).
[26] A. R. Wright, Sci. Rep. **3** (2013).
[27] M. Hohenadler, T. C. Lang, and F. F. Assaad, Phys. Rev. Lett. **106**, 100403 (2011), erratum **109**, 229902(E) (2012).
[28] D. Zheng, G.-M. Zhang, and C. Wu, Phys. Rev. B **84**, 205121 (2011).
[29] M. Hohenadler, Z. Y. Meng, T. C. Lang, S. Wessel, A. Muramatsu, and F. F. Assaad, Phys. Rev. B **85**, 115132 (2012).
[30] F. F. Assaad and H. G. Evertz, in *Computational Many Particle Physics*, Lecture Notes in Physics, Vol. 739, edited by H. Fehske, R. Schneider, and A. Weiße (Springer Verlag, Berlin, 2008) p. 277.
[31] A. N. Rubtsov, V. V. Savkin, and A. I. Lichtenstein, Phys. Rev. B **72**, 035122 (2005).
[32] M. Hohenadler and F. F. Assaad, Phys. Rev. B **85**, 081106 (2012), erratum **86**, 199901(E) (2012).
[33] E. Prodan, Phys. Rev. B **83**, 235115 (2011).
[34] B. Leung and E. Prodan, Phys. Rev. B **85**, 205136 (2012).
[35] M. Wimmer, ACM Trans. Math. Softw. **38**, 30 (2012).
[36] S. Rachel and K. Le Hur, Phys. Rev. B **82**, 075106 (2010).
[37] M. Laubach, J. Reuther, R. Thomale, and S. Rachel, arXiv:1312.2934 (2013).
[38] The color schemes are based on gnuplot-colorbrewer; 10.5281/zenodo.10282.
[39] H.-H. Hung, V. Chua, L. Wang, and G. A. Fiete, Phys. Rev. B **89**, 235104 (2014).
[40] H. Jiang, H. Liu, J. Feng, Q. Sun, and X. C. Xie, Phys. Rev. Lett. **112**, 176601 (2014).
[41] D. N. Sheng, Z. Y. Weng, L. Sheng, and F. D. M. Haldane, Phys. Rev. Lett. **97**, 036808 (2006).
[42] D. Sénéchal, arXiv:cond-mat/9908262v1 (1999).
[43] Y. Tanaka and N. Nagaosa, Phys. Rev. Lett. **103**, 166403 (2009).
[44] E. Orignac, M. Tsuchiizu, and Y. Suzumura, Phys. Rev. B **84**, 165128 (2011).
[45] Y. Tada, R. Peters, M. Oshikawa, A. Koga, N. Kawakami, and S. Fujimoto, Phys. Rev. B **85**, 165138 (2012).
[46] C.-H. Chung, D.-H. Lee, and S.-P. Chao, arXiv:1401.4875 (2014).
[47] J. von Delft and H. Schoeller, Annalen der Physik **7**, 225 (1998).
[48] F. D. M. Haldane, Journal of Physics C: Solid State Physics **14**, 2585 (1981).
[49] E. Orignac, M. Tsuchiizu, and Y. Suzumura, Phys. Rev. A **81**, 053626 (2010).
[50] K. S. D. Beach, eprint arXiv:cond-mat/0403055 (2004).
[51] T. Giamarchi, *Quantum Physics in One Dimension* (Oxford University Press, Oxford UK, 2004).
[52] A. Luther and I. Peschel, Phys. Rev. B **12**, 3908 (1975).
[53] E. Tang and L. Fu, arXiv:1403.7523v1 (2014).
[54] N. Goldman, I. Satija, P. Nikolic, A. Bermudez, M. A. Martin-Delgado, M. Lewenstein, and I. B. Spielman, Phys. Rev. Lett. **105**, 255302 (2010).
[55] N. R. Cooper, Phys. Rev. Lett. **106**, 175301 (2011).
[56] M. Aidelsburger, M. Atala, S. Nascimbène, S. Trotzky, Y.-A. Chen, and I. Bloch, Phys. Rev. Lett. **107**, 255301 (2011).
[57] S. K. Baur, M. H. Schleier-Smith, and N. R. Cooper, arXiv:1402.3295 (2014).
[58] A. Celi, P. Massignan, J. Ruseckas, N. Goldman, I. B. Spielman, G. Juzeliunas, and M. Lewenstein, Phys. Rev. Lett. **112**, 043001 (2014).